

# On the sensitivity of aerosol-cloud interactions to changes in sea surface temperature in radiative-convective equilibrium

Suf Lorian<sup>1,2</sup> and Guy Dagan<sup>1</sup>

<sup>1</sup>Fredy and Nadine Herrmann Institute of Earth Sciences, The Hebrew University of Jerusalem, Jerusalem, Israel

<sup>2</sup>The Racah Institute of Physics, The Hebrew University of Jerusalem, Jerusalem, Israel

**Correspondence:** Guy Dagan (guy.dagan@mail.huji.ac.il)

**Abstract.** Clouds play a vital role in regulating Earth’s energy balance, and are impacted by anthropogenic aerosol concentration ( $N_a$ ) and sea surface temperature (SST) alterations. Traditionally, these factors, aerosols and SST, are investigated independently. This study employs cloud-resolving, radiative-convective-equilibrium (RCE) simulations to explore aerosol-cloud interactions (ACIs) under varying SSTs. ACIs are found to be SST-dependent even under RCE conditions. Notably, changes in cloud radiative effects for both the longwave and shortwave radiations lead to a decrease in top-of-atmosphere (TOA) energy gain with increasing  $N_a$ . The changes in TOA shortwave flux exhibit greater sensitivity to underlying SST conditions compared to longwave radiation, due to changes in the cloud fraction. To comprehend these trends, we perform a linear decomposition, analyzing the responses of different cloud regimes and contributions from changes in cloud’s opacity and occurrence. This breakdown reveals that ice and shallow clouds predominantly contribute to the radiative effect, mostly due to changes in cloud’s opacity, due to the Twomey effect. Moreover, with an increase in  $N_a$ , we observe an increase in latent heat release at the upper troposphere associated with heightened production of snow and graupel. We show that this trend, consistently across all SSTs, affects the anvil cloud cover by affecting the static–stability at the upper troposphere via a similar mechanism to the iris–stability effect, resulting in a decline in TOA longwave energy gain. In conclusion, under the ongoing climate change, studying the sensitivity of clouds to aerosols and SST should be conducted concomitantly as mutual effects are expected.

## 1 Introduction

The response of clouds to anthropogenic perturbations is highly uncertain, posing a significant challenge in predicting future climate. This uncertainty stems mainly from two aspects: 1) uncertainty regarding the change in top-of-atmosphere (TOA) radiative flux resulting from the cloud response to warming, referred to as cloud feedback (Ceppi et al., 2017), and 2) uncertainty regarding the response of clouds to anthropogenic aerosols (Bellouin et al., 2020). In the latter case, aerosols, which can serve as cloud condensation nuclei (CCN) and ice nuclei, could affect the microphysical properties and processes in clouds (Bellouin et al., 2020). Specifically, clouds forming under higher aerosol concentrations (polluted clouds) usually have initially smaller and more numerous droplets, with a narrower size distribution compared to clean clouds (Squires, 1958; Squires and Twomey, 1960). The initial droplet size distribution affects the cloud’s albedo (Twomey, 1974, 1977; Bellouin et al., 2020) and

25 can affect key cloud processes such as condensation–evaporation, collision–coalescence and sedimentation (Albrecht, 1989; Seinfeld et al., 2016; Dagan et al., 2017; Heikenfeld et al., 2019; Christensen et al., 2022). These effects are known to be dependent on the environmental conditions (Gryspeerd and Stier, 2012; Christensen et al., 2016; Dagan and Stier, 2020b), hence are expected to be state/time-dependent under ongoing climate change (Dagan et al., 2017; Igel and van den Heever, 2021; Dagan, 2022).

30 Ultimately, the microphysical effects mentioned above could modify the precipitation production (Albrecht, 1989). Specifically, the initiation of warm rain has been shown to be delayed and to start at higher elevations under more polluted conditions (Rosenfeld, 2000; Freud and Rosenfeld, 2012; Dagan et al., 2015; Heikenfeld et al., 2019). However, in deep convective clouds, the precipitation production could be compensated — or even over-compensated — for at higher levels of the clouds to which more water is advected under more polluted conditions (Rosenfeld et al., 2008; Koren et al., 2014; Altaratz et al., 2014). As the  
35 freezing level elevation increases with sea surface temperature (SST), at lower SSTs the warm layer (containing liquid only) of a deep convective cloud is narrower in comparison to higher SSTs. Thus, an aerosol perturbation is hypothesized to more likely suppress warm rain completely at lower SSTs than at higher SSTs, where the relatively deep warm layer of the clouds enables longer diffusional growth of the droplets to the critical size which initiates precipitation (Freud and Rosenfeld, 2012; Heikenfeld et al., 2019). Warm rain suppression and, as a consequence, enhanced freezing of this water in the cold (containing  
40 ice) sections of the cloud, will result in more latent heat release at the upper parts of the troposphere (Rosenfeld et al., 2008; Igel and van den Heever, 2021) and thus in changes in the atmospheric stability.

In addition to the effect on precipitation, it has been previously suggested that the aerosol’s effect on deep convective clouds can increase the anvil cloud mass and extent by increasing the upward advection of water (Fan et al., 2010, 2013; Grabowski and Morrison, 2016; Chen et al., 2017). This trend could be explained by the convective invigoration hypothesis (Williams  
45 et al., 2002; Koren et al., 2005; Seifert and Beheng, 2006; Rosenfeld et al., 2008; Yuan et al., 2011; Koren et al., 2014). Under this hypothesis, which remains highly questionable, increasing aerosol concentrations have been suggested to drive stronger latent heat release and hence stronger vertical velocities. In addition, under high aerosol concentration conditions, the smaller hydrometeors are transported higher into the atmosphere for a given vertical velocity (Koren et al., 2015; Dagan et al., 2018, 2020), and their lifetime at the upper troposphere is longer, due to a weaker sedimentation rate (Fan et al., 2013;  
50 Grabowski and Morrison, 2016). However, it is important to note that these proposed aerosol effects are still highly uncertain (Stevens and Feingold, 2009; Varble, 2018; Romps et al., 2023).

Cloud feedback, or the response of the cloud radiative effect (CRE) to surface warming, was recently shown to depend on the assumed aerosol concentration (Dagan, 2022). In the tropics, the radiative effect of both shallow (Gettelman and Sherwood, 2016) and deep (Ceppi et al., 2017) clouds is expected to further warm the surface. Shallow tropical and sub-tropical clouds  
55 — which have a general radiative cooling effect — are expected to become less prevalent and less radiatively opaque, thus producing a positive (but still highly uncertain) feedback (Gettelman and Sherwood, 2016; Nuijens and Siebesma, 2019). At the same time, deep tropical clouds are also expected to react to surface warming in a way that modifies their CRE (Ceppi et al., 2017). Specifically, it has been suggested that the tropical anvil cloud temperature and coverage react to surface warming (Hartmann and Larson, 2002; Zelinka and Hartmann, 2010; Bony et al., 2016; Ceppi et al., 2017). Tropical anvil clouds

60 strongly modulate the longwave emissions of Earth as these clouds are much colder than the surface (by about 70-90K) and  
 are generally opaque in the longwave, thus emitting a significantly lower amount of energy to space than otherwise would be  
 emitted without them. In addition, anvil clouds could also strongly modulate the shortwave radiation budget, depending on  
 their optical thickness (Hartmann and Berry, 2017; Li et al., 2019; Sokol, 2024). Hence, any anthropogenic-driven changes  
 to the anvil cloud properties, such as amount and temperature, could significantly affect Earth’s energy budget (Zelinka and  
 65 Hartmann, 2010; Ceppi et al., 2017).

A central feature of the anvil cloud response to SST changes is the fixed anvil temperature (FAT) hypothesis (Hartmann  
 and Larson, 2002), which states that the temperature of anvil clouds is anticipated to remain roughly fixed with warming.  
 According to the FAT hypothesis, anvil top heights are determined by clear-sky radiative cooling, which in turn is primarily  
 determined by water vapor concentration. The water vapor concentration, following the Clausius-Clapeyron relation, sharply  
 70 drops to negligible values near the temperatures of the upper-troposphere, making the radiative cooling inefficient above this  
 level and still efficient below this level. In a clear-sky free troposphere, radiative cooling is balanced by adiabatic warming due  
 to subsiding motions, thus the energy budget can be formulated as follows:

$$Q_r = -S\omega \quad (1)$$

where  $Q_r$  is the radiative cooling rate,  $\omega$  is the clear sky vertical pressure velocity, and  $S$  is the static-stability defined as:

$$S = -\frac{T}{\theta} \frac{\partial \theta}{\partial P} \quad (2)$$

where  $T$  is the air temperature,  $\theta$  is the potential temperature and  $P$  is the pressure.

75 The subsidence motion below the sharp drop in radiative cooling and the lack of subsidence above this level generates vertical  
 divergence in the clear sky, which, due to conservation of mass, is balanced by horizontal divergence from the convective  
 regions. This convective divergence controls anvil clouds (Hartmann and Larson, 2002; Zelinka and Hartmann, 2011, 2010;  
 Bony et al., 2016) (Below, in Fig. 7, vertical profiles of  $S$ ,  $Q_r$ ,  $\omega$  and its vertical divergence are presented).

While observations, global climate models and high-resolution, convective-permitting models predict an increase in altitude  
 80 of anvil clouds while maintaining nearly fixed temperatures, they also anticipate a decrease in anvil cloud coverage with rising  
 surface temperatures (Lindzen et al., 2001; Zelinka and Hartmann, 2011; Mauritsen and Stevens, 2015; Bony et al., 2016;  
 Williams and Pierrehumbert, 2017; Wing et al., 2020; Saint-Lu et al., 2020; Beydoun et al., 2021). The mechanisms behind  
 this decrease in anvil cloud coverage rely on the same physics as do the mechanisms of the FAT hypothesis. Namely, it has  
 been suggested that as the climate warms, the clouds rise, but find themselves in a more stable atmosphere (while remaining  
 85 at nearly the same temperature). This enhanced stability under warmer conditions reduces the convective outflow in the upper  
 troposphere and hence decreases the anvil cloud fraction (Bony et al., 2016; Beydoun et al., 2021). Specifically, it was shown  
 that the maximum of the radiative-driven mass divergence in convective regions ( $D_r$ ), defined as:

$$D_r = \frac{\partial \omega}{\partial P} \quad (3)$$

can accurately predict the anvil cloud fraction, and decreases with the increase in stability occurring with an increase in SST  
 (Bony et al., 2016; Beydoun et al., 2021). In addition to the radiative-driven divergence, slow evaporation (Seeley et al., 2019)

90 and sedimentation (Beydoun et al., 2021) of the ice crystals at the upper troposphere contribute to anvil cloud formation. However, changes in the lifetime of anvil clouds — determined by changes in sedimentation and evaporation — were shown to play a secondary role in the response of anvil clouds to warming (Beydoun et al., 2021).

In this study, we focus on the synergistic SST and aerosol effects on tropical convective clouds, and specifically on the CRE, under equilibrium conditions using idealized cloud-resolving, radiative-convective-equilibrium (RCE) simulations. This is done following previous studies that uses RCE to examine different aspects of ACI (van den Heever et al., 2011; Storer and van den Heever, 2013; Beydoun and Hoose, 2019; Dagan, 2022).

## 2 Methods

### 2.1 Model description

The model used in this study is the System for Atmospheric Modeling (Khairoutdinov and Randall, 2003, SAM) version 6.11.7. The microphysics scheme used is the two-moment bulk microphysics of Morrison et al. (2005). The aerosols available for activation are represented by a power law function of the super-saturation ( $SS$ ):  $CCN = N_a SS^k$ , where  $N_a$  is the concentration of CCN available at 1% super-saturation and  $k$  is a constant, here equal to 0.4, representing typical maritime conditions. CCN activation at the cloud base is parameterized using the vertical velocity and CCN spectrum parameters (Twomey, 1959). In this case, we use different  $N_a$  concentrations for representing changes in aerosol concentration. Here, ice nucleation is not directly coupled to  $N_a$  (i.e., changes in  $N_a$  do not change the concentration of ice nucleating particles- INP), but rather depends on the temperature and the supersaturation with respect to ice (Rasmussen et al., 2002). We note that, in realistic conditions, changes in  $N_a$  might cause changes in INP, an effect that should be addressed in future research. In our simulations, heterogeneous nucleation dominates for temperatures higher than approximately 238 K, while ice formation is dominated by homogeneous freezing for temperatures lower than approximately 233 K (Rasmussen et al., 2002). Ice nucleation directly from vapor is not considered here. Direct interactions between aerosols and radiation are also not considered here, however, aerosols could affect the radiation via modifying the clouds' properties. In order to represent the Twomey effect (Twomey, 1977), the model is configured to pass cloud water and ice-crystal effective radii from the microphysics scheme to the radiation scheme.

### 2.2 Experimental design

The simulations used here generally follow the Radiative-Convective-Equilibrium Model Intercomparison Project (Wing et al., 2018, RCEMIP) small domain protocol but with changes in aerosol concentration. The simulations are run in a small domain, of  $96 \times 96$  km<sup>2</sup>, in order to avoid the effects of convective self-aggregation (Muller and Held, 2012; Lutsko and Cronin, 2018). The simulations are conducted with a horizontal grid spacing of 1 km, 68 vertical levels between 25 m and 31 km, and a vertical grid spacing increasing from 50 m at the surface to around 1 km at the domain top. To get solar insolation close to the tropical-mean value, the solar radiation is fixed at 551.58 W m<sup>-2</sup>, with a zenith angle of 42.05° (Wing et al., 2018). A diurnal cycle is not considered here, and we note that it might affect the convective development to some extent even over the ocean



(Nesbitt and Zipser, 2003; Gasparini et al., 2022). In order to initialize convection, a small thermal noise is added near the surface at the beginning of each simulation.

The concentration of CO<sub>2</sub> is fixed at the pre-industrial level (280 ppm), while there are 25 different  $N_a$  and SSTs combinations, 5 different values for each.  $N_a$  ranges from 20 to 2000 cm<sup>-3</sup> (20, 100, 200, 1000, and 2000 cm<sup>-3</sup>), following a recent observational data set (Choudhury and Tesche, 2023), which showed the feasibility of this  $N_a$  range. The SST ranges from 290 to 310 K in 5 K intervals. This wide range of aerosol and SST conditions are used to maximize the effects and for establishing a better physical understanding. A fixed ozone profile, representing a typical tropical atmosphere, is used here (Wing et al., 2018). We note that using a fixed ozone profile under different SSTs is not entirely realistic and may have some effect on the clouds development (Harrop and Hartmann, 2012; Seidel and Yang, 2022). For simplicity, the effect of other trace gases (such as CH<sub>4</sub> and N<sub>2</sub>O) is neglected. The temporal resolution of the simulations is 10 seconds, and of the interactive radiative scheme is 5 minutes (using the CAM radiation scheme (Collins et al., 2006)). All fields have an output resolution of 1 hour; 3-D fields are saved as snapshots, while domain statistics are saved as hourly averages. Each simulation was run for 150 days (Wing et al., 2018), and the last 30 days of each simulation were used for statistical analysis.

### 3 Results and discussion

#### 3.1 Response of the domain mean properties to aerosol perturbation under different SSTs

We start by examining the effect of changes in  $N_a$  on the TOA energy gain under different SSTs ( $\Delta R$ ; Fig. 1a). This figure illustrates that for all SSTs, an increase in  $N_a$  decreases  $\Delta R$ , an effect which becomes stronger with a decrease in the SST. Both the longwave (LW) and shortwave (SW) components of  $\Delta R$  are negatively affected by  $N_a$  (each declining up to 4–5 W m<sup>-2</sup> for the entire  $N_a$  range considered here, depending on the SST; Fig. 1b and c), with  $\Delta R^{SW}$  being more susceptible to SST changes (Fig. 1c), and  $\Delta R^{LW}$  decreases in a roughly similar manner across all SSTs (Fig. 1b). Moreover, the CRE (calculated as all sky radiative flux minus clear sky radiative flux) is identified as the main driver of  $\Delta R$  variations, while changes in clear sky radiation has a minimal impact, as indicated by Fig. 1d-f. This is true in our simulations as changes in  $N_a$  do not directly affect radiation by aerosol-radiation interactions.

In order to understand the radiative effect of an increase in  $N_a$  under the different SSTs, we first examine the domain- and time-mean cloud liquid water path, ice water path and cloud fraction ( $\mathcal{L}$ ,  $\mathcal{I}$  and CF respectively; Fig. 2). This Figure illustrates a monotonic increase in  $\mathcal{L}$  with  $N_a$ , which is generally stronger under lower SSTs, and a monotonic decrease in both  $\mathcal{I}$  and CF, consistently across SSTs.

Next, we examine vertical profiles of the different hydrometeors (Fig. 3). We note that with an increase in SST, the freezing level increases. Since an increase in  $N_a$  acts to push warm rain formation to higher levels (Rosenfeld, 2000; Freud and Rosenfeld, 2012; Heikenfeld et al., 2019), under lower SSTs, for which the freezing level is relatively shallow (about 1250 m above cloud base in the coldest case considered here), an increase in  $N_a$  can inhibit warm rain (Fig. 3g). In contrast, under higher SSTs, for which the freezing level is relatively deep (about 6000 m above cloud base in the warmest case considered here), an increase in  $N_a$  drives warm rain inhibition at the lower levels, which is compensated for at higher levels of the warm section

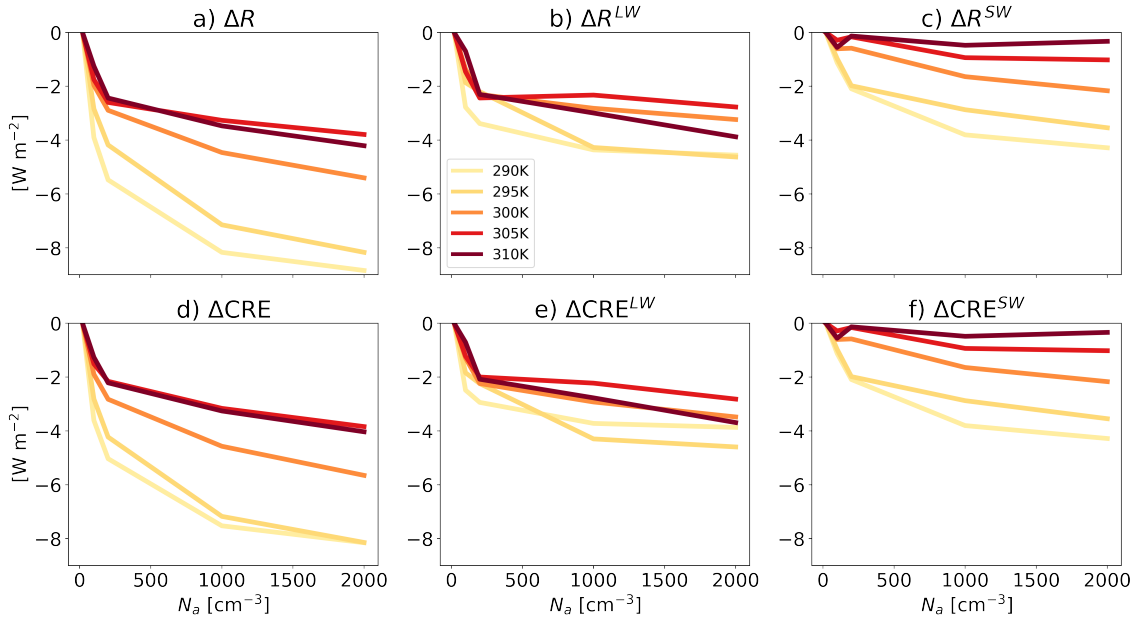


**Figure 1.** Changes in the domain and time mean radiative fluxes at the top of the atmosphere due to changes in aerosol concentrations ( $N_a$ ). (a) presents the total change in radiation, while (b) and (c) present changes in longwave (LW) and shortwave (SW) radiation, respectively. (d-f) present the changes in the total cloud radiative effect (CRE) and its LW and SW components, respectively. The values are presented relative to the cleanest run ( $N_a = 20 \text{ cm}^{-3}$ ) for each SST, as indicated by the  $\Delta$  sign.

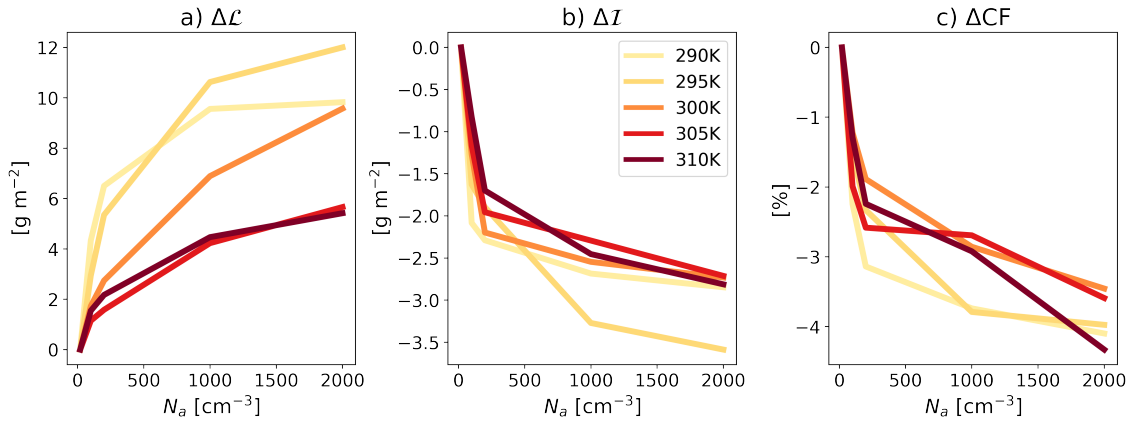


**Figure 2.** The response of domain and time mean liquid water path ( $\mathcal{L}$ ; a), ice water path ( $\mathcal{I}$ ; b) and cloud fraction (CF; c) to an increase in  $N_a$ . The values are presented relative to the cleanest run ( $N_a = 20 \text{ cm}^{-3}$ ) for each SST, as indicated by the  $\Delta$  sign.

(Fig. 3g). That is to say that under low SSTs, the delay in warm rain is not being offset at higher levels within the warm section,

155 while under high SSTs we do see such an offset. This explains the stronger rise in water content within the warm section ( $\mathcal{L}$ ) with an increase in  $N_a$  (Albrecht, 1989) under low SST conditions compared to high SST conditions (Fig. 2a).

Beside resulting in an increase in  $\mathcal{L}$ , the warm rain inhibition under higher  $N_a$  results in more super-cooled water (Carrió et al., 2011; Chen et al., 2017, Fig. 3f), leading to higher production of snow (Chen et al., 2017, Fig. 3j), and drives higher riming rates, thus producing more graupel (Chen et al., 2017, Fig. 3i). We will get back to this observed trend for the explanation of the results presented in Fig. 10 below. In addition, cloud ice declines with  $N_a$ , consistently across SSTs (Fig. 3h). This trend is consistent with the decline in  $\mathcal{I}$  and CF (2b and c, respectively) and will be discussed further below (Fig. 6d).

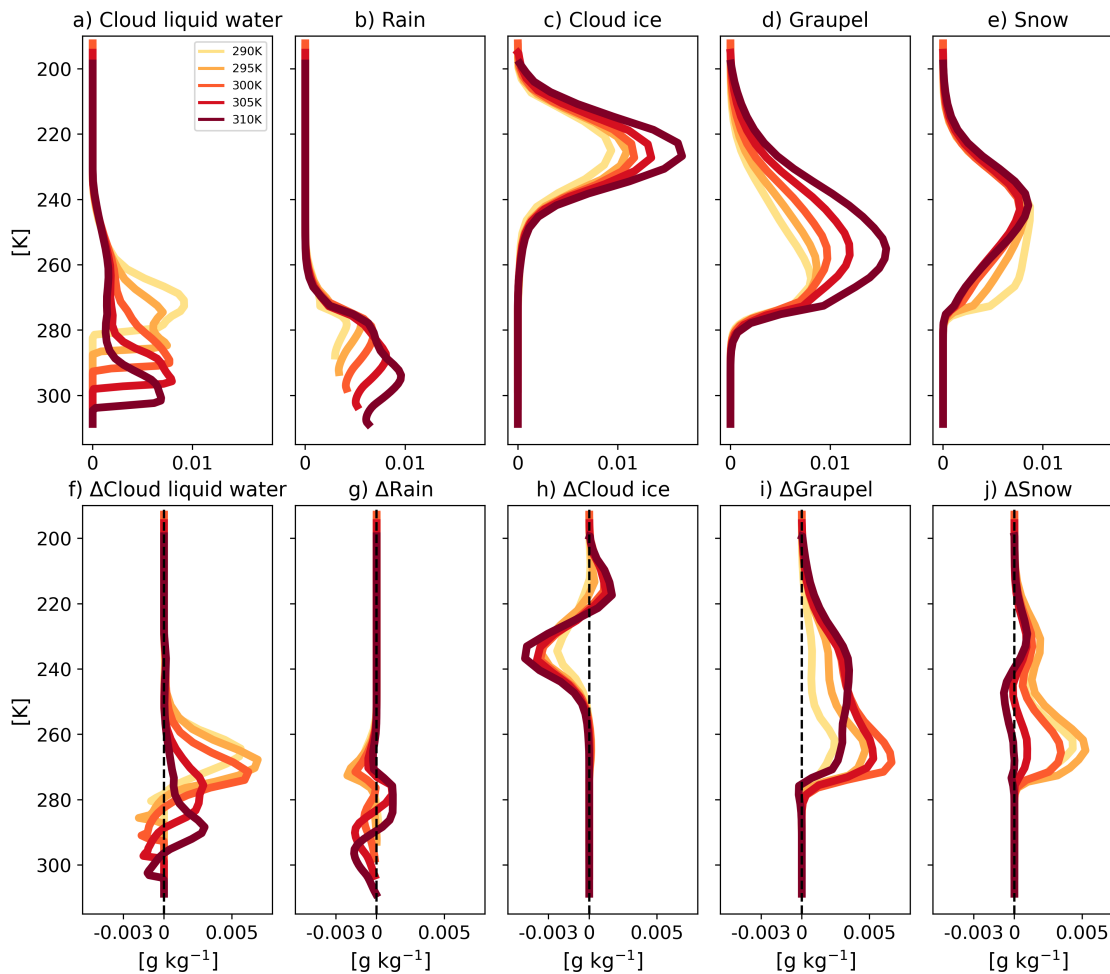


**Figure 3.** Domain and time mean vertical profiles of the different hydrometeors for the cleanest runs ( $N_a = 20 \text{ cm}^{-3}$ ): (a) cloud liquid water, (b) rain, (c) ice, (d) graupel, and (e) snow, and their response to increasing  $N_a$  to  $2000 \text{ cm}^{-3}$ , relative to the cleanest run for each SST (f – j). Here we only present the cleanest and the response of the most polluted runs for clarity. The full range of  $N_a$  is presented in Figs. S1-S5, SI.

### 3.2 Response by cloud regimes

Figs. 1, 2 and 3 examine the bulk cloud and radiative properties in the domain. However, as previously demonstrated, the impact of aerosols on clouds is cloud regime dependent (Gryspeerd and Stier, 2012; Christensen et al., 2016; Dagan and Stier, 165 2020b). Therefore, it is crucial to analyze the distribution of cloud regimes in our simulations and discern how each specific cloud regime responds to the increase in  $N_a$ . In this paper we define the cloud regimes based on different bins of  $\mathcal{L}$  and  $\mathcal{I}$ . For that purpose, Fig. 4 presents 2D histograms of the cloud fraction (CF), or cloud occurrence, at the different bins of  $\mathcal{L}$  and  $\mathcal{I}$  and the average total, shortwave and longwave CRE at these different bins, all for the coldest case considered here (SST = 290 K) as an example. This figure illustrates that the CF in these RCE simulations is mostly dominated by anvil clouds (e.g. 170 Wing et al. (2020)), i.e., clouds with negligible  $\mathcal{L}$  and high (thick anvil clouds; denoted by marker 1 in Fig. 4a) or low (thin anvil clouds; denoted by marker 2 in Fig. 4a)  $\mathcal{I}$ . We note that the average CRE of thin anvil cloud is small but not positive as in previous assessments (Sokol, 2024), probably due to the use of a relatively coarse resolution of  $\mathcal{L}$  and  $\mathcal{I}$  bins. However, Fig. 4a also illustrates the existence of two other types of clouds in these RCE simulations - shallow clouds (high  $\mathcal{L}$  and low  $\mathcal{I}$ ; denoted by marker 3 in Fig. 4a) and deep convective cores (high  $\mathcal{L}$  and high  $\mathcal{I}$ ; denoted by marker 4 in Fig. 4a). In addition, 175 Fig. 4 i-l illustrates the difference between simulations with the highest ( $2000 \text{ cm}^{-3}$ ) and the lowest ( $20 \text{ cm}^{-3}$ )  $N_a$  conditions. Specifically, Fig. 4i illustrates that an increase in  $N_a$  drives thinning of the anvil clouds, i.e., an increase in the frequency of thin anvil clouds and a decrease in the frequency of thick anvil clouds. Furthermore, Fig. 4 j-l illustrate that with an increase in  $N_a$  the CRE decreases for all  $\mathcal{L}$  and  $\mathcal{I}$  bins (and especially for medium-high  $\mathcal{L}$  and low  $\mathcal{I}$ ; Fig. 4j), driven mostly by changes in the SW (Fig. 4k), with only minor changes in the LW (Fig. 4l). This SW difference with  $N_a$  can be explained by the Twomey 180 effect (Twomey, 1974).

Following the method outlined in Sokol (2024), we calculate the total ice cloud fraction ( $CF_{ice}$ ) as the integral over thick ice plus thin ice regimes as defined in Table S1, SI. Fig. 5a illustrates a (mostly) monotonic decrease across SSTs in  $CF_{ice}$  with increasing  $N_a$ , consistent with the domain mean CF reduction (Fig. 2c). We note that not just the integrated  $CF_{ice}$  decreases with  $N_a$ , but the entire distribution of  $\mathcal{I}$  is shifted to lower values (i.e., thinning of the anvil clouds; Figs. 4i, 2b and 3h). A 185 decrease in  $CF_{ice}$  leads to more outgoing LW radiation out of the atmosphere and reduces  $\Delta R^{LW}$ , as can be seen in Fig. 1b. In addition, Fig. 5b presents the relative change in the shallow cloud fraction ( $CF_{shallow}$ ; calculated as the integral over the shallow regime as defined in Table S1, SI). We note that this definition of shallow clouds might also include two-layer cloud conditions with cirrus clouds with relatively low  $\mathcal{I}$  above shallow clouds. Figure 5b illustrates a rise in  $CF_{shallow}$  with  $N_a$  for low SST, while for high SST it illustrates a decrease in  $CF_{shallow}$  with  $N_a$  (the change in the shallow cloud fraction 190 is not observed in Fig. 4i due to the dominance of ice clouds, which inflates the color-bar range). We note that although the relative changes in  $CF_{ice}$  and  $CF_{shallow}$  has similar magnitudes, the baseline (i.e., referring to the simulated value, and not the difference between the most polluted and cleanest runs)  $CF_{ice}$  is two orders of magnitude larger than  $CF_{shallow}$  (Fig. S6, SI).

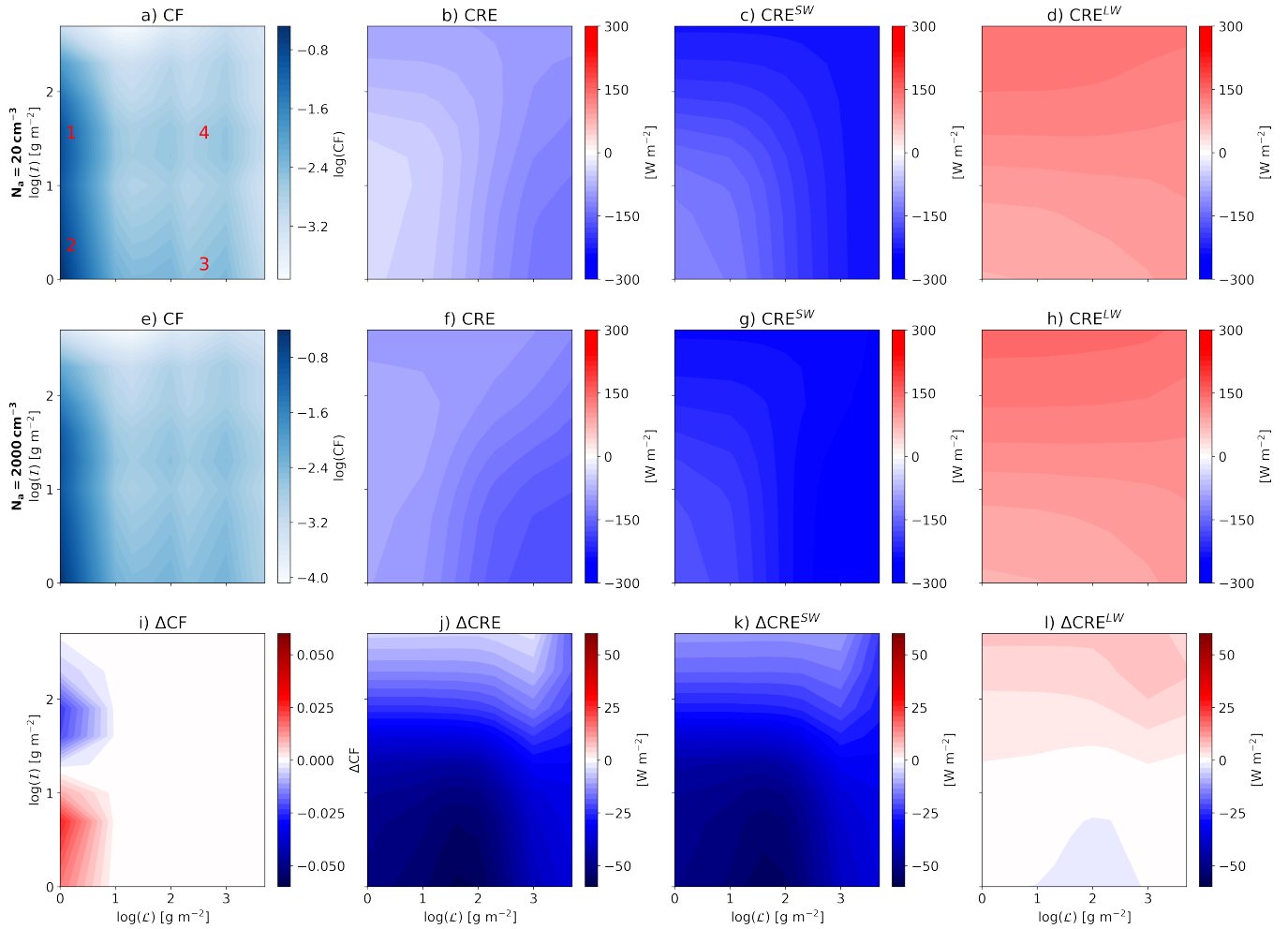


**Figure 4.** Domain and time mean two-dimensional histograms of cloud fraction (CF; **a** and **e**), at different bins of liquid water path ( $\mathcal{L}$ ) and ice water path ( $\mathcal{I}$ ) and the average total (**b** and **f**), shortwave (**c** and **g**) and longwave (**d** and **h**) cloud radiative effect (CRE) at these different bins. These quantities are presented for two simulations using the lowest ( $N_a = 20 \text{ cm}^{-3}$ ; **a-d**), and the highest ( $N_a = 2000 \text{ cm}^{-3}$ ; **e-h**)  $N_a$ , under SST = 290 K. In addition, the difference between the highest and lowest  $N_a$  conditions is presented in panels **i-l**.

Fig. 4 illustrates that the response of the CRE to an increase in  $N_a$  is driven both by changes in CF (Fig. 4i) and by changes in CRE for a given bin of  $\mathcal{L}$  and  $\mathcal{I}$  (Fig. 4j). Next, we aim to quantitatively separate these two effects. Thus, we write the total CRE as the integral over the different bins of  $\mathcal{L}$  and  $\mathcal{I}$  of the CF times the CRE in each bin:

$$CRE = \int_0^{\infty} \int_0^{\infty} CRE(\mathcal{L}, \mathcal{I}) CF(\mathcal{L}, \mathcal{I}) d\mathcal{L} d\mathcal{I} \quad (4)$$

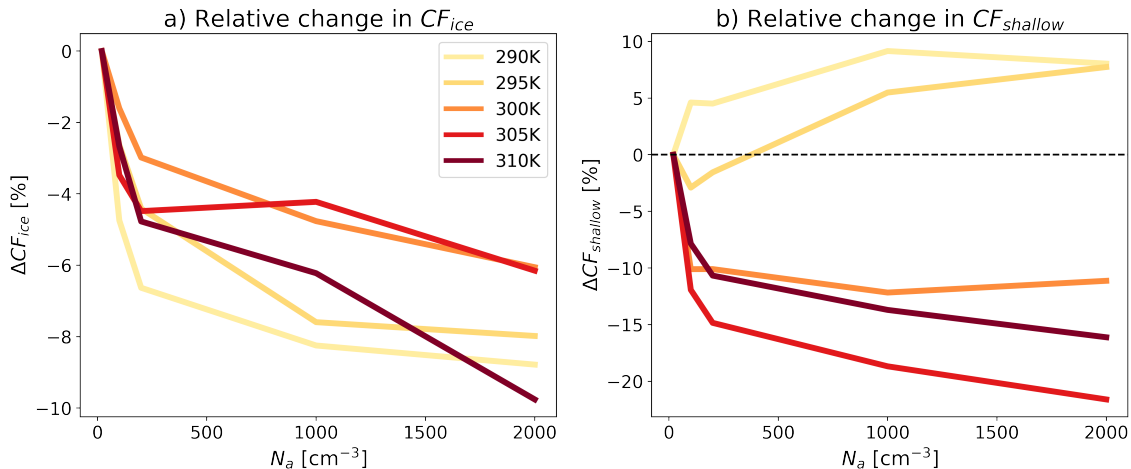


**Figure 5.** The relative response of domain and time mean ice cloud fraction ( $CF_{ice}$ ; **a**) and shallow cloud fraction ( $CF_{shallow}$ ; **b**) to an increase in  $N_a$ . The values are shown as a difference, relative to the cleanest run (as denoted by the  $\Delta$  sign), for each SST. The baseline  $CF_{ice}$  and  $CF_{shallow}$  are presented in Fig. S6, SI.

In the simulations presented here  $\Delta CRE \approx \Delta R$  (Fig. 1). Thus, following a somewhat similar method to that presented in Bony (2004) and Sokol (2024), we decompose the mean  $\Delta R$  into three contributions: a) changes in  $\Delta R$  due to changes in the cloud's opacity per  $\mathcal{L}$  and  $\mathcal{I}$  bin (the opacity term or the Twomey term), (b) a shift in the occurrence or CF in each  $\mathcal{L}$  and  $\mathcal{I}$  bin (the shift term or the  $\mathcal{L}/\mathcal{I}$  term), and (c) the combined effect of changes in the cloud's opacity and shift (the nonlinear term). Mathematically, this decomposition can be written as:

$$\begin{aligned}
 \Delta CRE &\approx \Delta R \\
 &= \underbrace{\int_0^\infty \int_0^\infty \Delta CRE(\mathcal{L}, \mathcal{I}) CF(\mathcal{L}, \mathcal{I}) d\mathcal{L} d\mathcal{I}}_{\text{Opacity}} \\
 &\quad + \underbrace{\int_0^\infty \int_0^\infty CRE(\mathcal{L}, \mathcal{I}) \Delta CF(\mathcal{L}, \mathcal{I}) d\mathcal{L} d\mathcal{I}}_{\text{Shift}} \\
 &\quad + \underbrace{\int_0^\infty \int_0^\infty \Delta CRE(\mathcal{L}, \mathcal{I}) \Delta CF(\mathcal{L}, \mathcal{I}) d\mathcal{L} d\mathcal{I}}_{\text{nonlinear}} \tag{5}
 \end{aligned}$$

The opacity term represents changes in the CRE while the CF and  $\mathcal{L}/\mathcal{I}$  distribution are held fixed, i.e., multiplying Fig. 4a with Fig. 4j, while the shift term represents changes in the CF while the CRE per  $\mathcal{L}$  and  $\mathcal{I}$  bin is held fixed, i.e., multiplying Fig. 4b with Fig. 4i. Lastly, the nonlinear term is acquired, for example, by multiplying Fig. 4i with Fig. 4j.

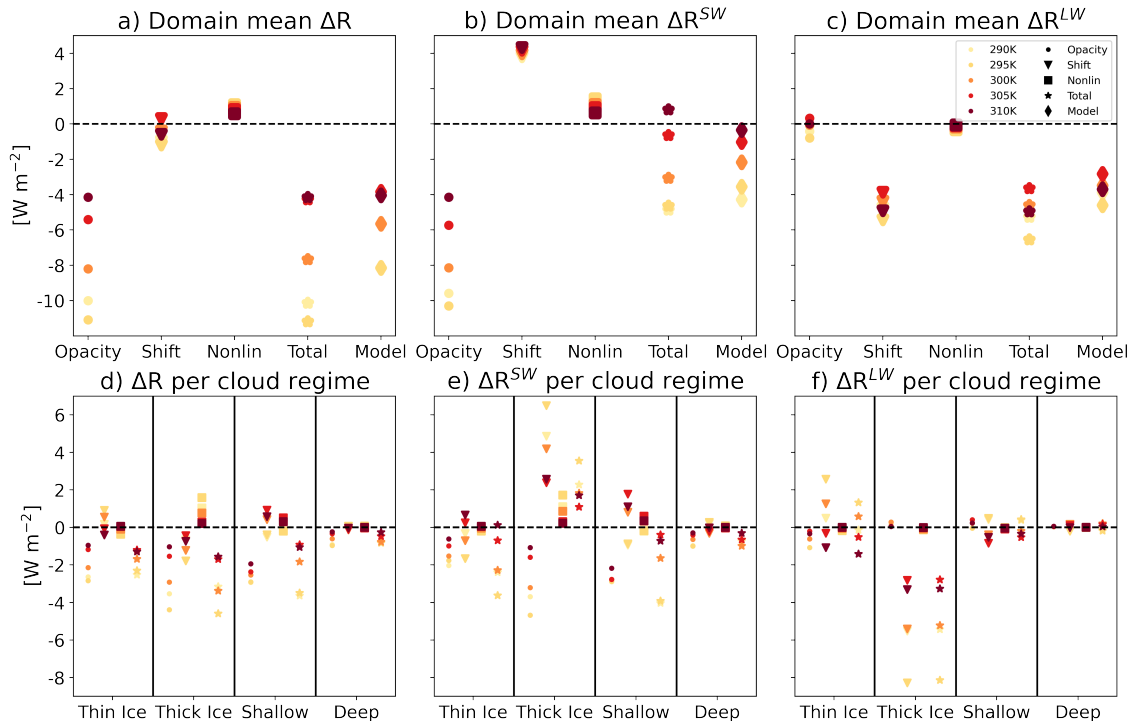


**Figure 6.** The response of time mean  $\Delta R$ ,  $\Delta R^{SW}$  and  $\Delta R^{LW}$  to an increase in  $N_a$  for the domain mean (a-c), and per cloud regime (d-f). The values shown are decomposed to the three terms shown in eq. 5 (Opacity, Shift and Nonlin), and the increase in  $N_a$  is represented by the difference between the most polluted run ( $N_a = 2000 \text{ cm}^{-3}$ ) and the cleanest run ( $N_a = 20 \text{ cm}^{-3}$ ), for each SST.

Fig. 6a-c illustrates the decomposition presented in eq. 5 for the domain mean (i.e., integrating over all  $\mathcal{L}$  and  $\mathcal{I}$  bins, excluding the no clouds regime as defined in Table S1, SI) for all the different SSTs. Fig. 6a-c also present the simulated response as presented in Fig. 1 (referred to as "Model") and the sum over the three terms presented in eq. 5 (referred to as "Total"). These panels illustrate that the opacity term is the main driver for the decline in  $\Delta R$  with  $N_a$  (Fig. 6a), occurring  
210 mostly through the SW (Fig. 6b). In addition, this figure illustrates that the opacity term is the main driver for the SST-sensitivity, demonstrating a generally weaker response as the SST increases, consistent with Fig. 1. The shift term, on the other hand, demonstrates similar magnitudes but opposite sign in the SW and LW (Figs. 6b and c, respectively), with a weak SST-dependence, thus making this term negligible in the total (Fig. 6a). The nonlinear term shows close to zero contributions to  $\Delta R$  and its SW and LW components, thus justifying focusing on the linear decomposition in eq. 5. We note that the decomposition  
215 results in a similar magnitude and SST-trend as the model (comparing Total to Model in Fig. 6a-c), thus justifying its use. However, we also note a slight over-estimation of  $\Delta R$  using the decomposition at the lower SSTs (Fig. 6a).

In addition to the domain mean,  $\Delta R$  is decomposed per cloud regime by integrating over the relevant part of the  $\mathcal{L}$  and  $\mathcal{I}$  phase-space (Fig. 6d-f and Table S1, SI). These panels illustrate that deep convective cores have negligible contributions to

$\Delta R$ ,  $\Delta R^{SW}$  and  $\Delta R^{LW}$ , mostly due to their small coverage (Fig. 4a). Therefore, most of the contribution to  $\Delta R$  comes from  
220 anvil and shallow clouds changes.

The thick and thin ice clouds' response drives a negative net total  $\Delta R$ , which is stronger under lower SSTs (Fig. 6d). This trend is dominated by the opacity term, which is driven almost entirely by the SW part of the spectrum (Fig. 6e). This term represents an increase in the reflectivity of the ice clouds for a given  $\mathcal{L}$  and  $\mathcal{I}$  distribution, and can be explained by a similar mechanism to the Twomey effect but for ice particles. This term becomes stronger (more negative) with a reduction in SST due  
225 to an increase in the baseline CF of these clouds (Fig. S6, SI). The shift term in thick ice clouds is strongly positive in the SW (Fig. 6e) and negative in the LW (Fig. 6f) due to the thinning of the ice clouds and the general reduction of the occurrence of these thick clouds (4i). However, the net effect of the shift term is low, for both thick and thin ice clouds, due to cancellation between the SW and the LW (Fig. 6d).

Similarly to the ice clouds' response, the shallow clouds' response also drives a negative net total  $\Delta R$ , which becomes  
230 stronger under lower SSTs (Fig. 6d). As expected, changes in shallow clouds have a small impact in the LW (Fig. 6f), but a significant effect in the SW (Fig. 6e). As in ice clouds, the negative net total  $\Delta R$  in the shallow clouds case is driven mostly by the opacity term, which in this case can be explained by the classical Twomey effect. Here again, the opacity term demonstrates a sensitivity to the underlying SST, and becomes stronger for lower SST due to an increase in the baseline CF (Fig. S6, SI). However, we note that the opacity term's SST-sensitivity cannot solely explain the SST-sensitivity in the total effect of shallow  
235 clouds (Fig. 6d). The shallow clouds' shift term also contributes to the total SST-sensitivity. This term, while having a relatively small magnitude, is negative under low SSTs and positive under high SSTs, consistent with the relative change in  $CF_{shallow}$ , which is positive under low SSTs and negative under high SSTs (Fig. 5b). The contrasting response of  $CF_{shallow}$  to  $N_a$  under the different SSTs can be explained by warm rain inhibition at varying depths of warm layers. As was noted above, with an increase in SST, the freezing level increases, while an increase in  $N_a$  acts to push warm rain formation to higher levels  
240 (Rosenfeld, 2000; Freud and Rosenfeld, 2012; Heikenfeld et al., 2019). Thus, under lower SSTs, for which the freezing level is relatively shallow, an increase in  $N_a$  can inhibit warm rain (see Fig. 3g) and hence lead to an increase in  $CF_{shallow}$ . In contrast, under higher SSTs, for which the freezing level is relatively deep, an increase in  $N_a$  drives warm rain inhibition at the lower levels, which is compensated for at higher levels of the warm section (Fig. 3g), thus eliminating the positive effect on  $CF_{shallow}$ .

245 The combined response of ice and shallow clouds to an increase in  $N_a$ , as explained in this section, can explain the reduction in  $\Delta R^{LW}$  with  $N_a$ , the reduction in  $\Delta R^{SW}$  with  $N_a$  and its SST-sensitivity, and hence the reduction in  $\Delta R$  with  $N_a$  and its SST-sensitivity (Fig. 1).

### 3.3 Mechanism behind the $CF_{ice}$ response to $N_a$

As was noted above, a decrease in  $CF_{ice}$  with  $N_a$  (Fig. 5a) leads to more outgoing LW radiation out of the atmosphere (Fig.  
250 1b). In order to understand the reduction in  $CF_{ice}$  and the ice cloud thinning with  $N_a$ , next we examine the sensitivity of the maximum (in the vertical dimension – see Fig. 7d) of the radiative-driven mass divergence (Bony et al., 2016,  $D_r$ ) to  $N_a$  under the different SSTs (Fig. 8). Fig. 8a illustrates that the  $CF_{ice}$  is strongly correlated with  $D_r$  (Pearson correlation coefficient  $\approx$



0.92 with P-value < 0.01). While the general decrease in  $D_r$  with SST has previously been demonstrated (Bony et al., 2016), here we show that for a given SST,  $D_r$  generally decreases with  $N_a$  (Fig. 8b). The general reduction in  $D_r$  with  $N_a$  drives a general reduction in  $CF_{ice}$  with  $N_a$  for a given SST (Figs. 5a and 8c). This reduction in  $D_r$  and  $CF_{ice}$  with  $N_a$  explains the reduction in  $\mathcal{I}$  and ice cloud (Figs. 2b and 3i, respectively) with  $N_a$ , which in turn can explain the reduction in  $\Delta R^{LW}$  (Fig. 1b).

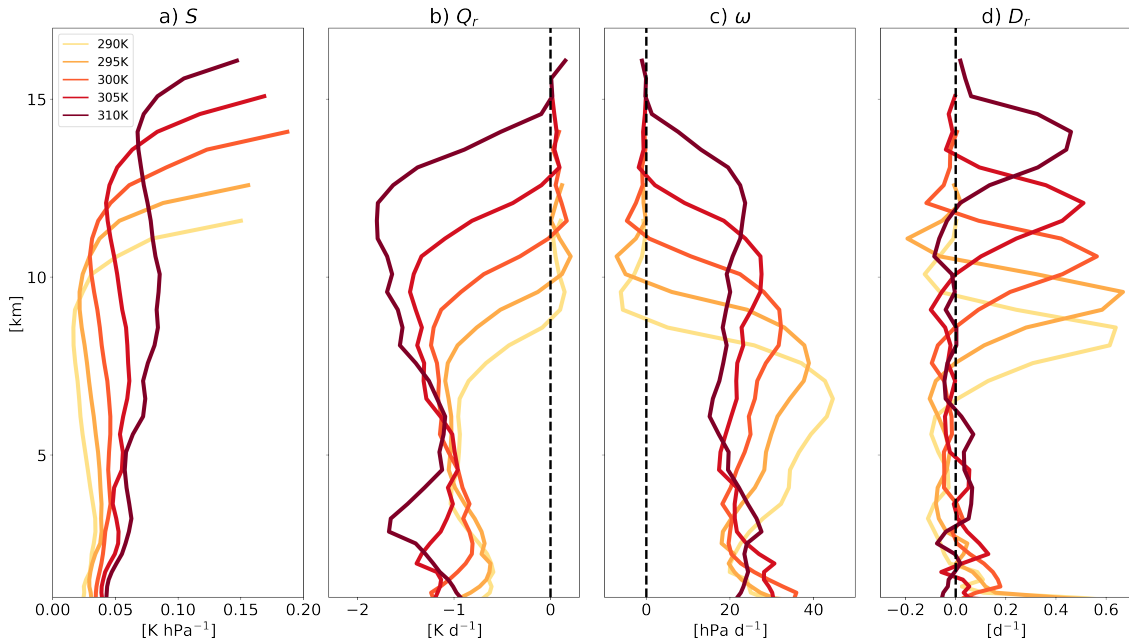


**Figure 7.** Domain and time mean vertical profiles of the: **a)** static-stability –  $S$ , **b)** radiative cooling rate –  $Q_r$ , **c)** vertical pressure velocity –  $\omega$ , and **d)** radiative-driven mass divergence –  $D_r$  for the different simulations conducted under  $N_a = 20 \text{ cm}^{-3}$  and different SST conditions.

In addition to modifying  $D_r$ , an increase in  $N_a$  also affects the lifetime of anvil clouds by perturbing the sedimentation rate (Grabowski and Morrison, 2016). Specifically, high aerosol conditions lead to smaller ice crystals, which sediment slower from the cloud (i.e. the sedimentation flux becomes less negative; Fig. S11, SI), thus acting to increase  $CF_{ice}$ . However, Fig. 5a shows a decrease in  $CF_{ice}$  with  $N_a$  in our simulations, thus making this to be only a secondary effect compared with the effect of  $D_r$  (agreeing with previous results regarding the effect of warming on anvil clouds (Beydoun et al., 2021)).

A reduction in  $D_r$  with  $N_a$  could be attributed to changes in  $Q_r$  (the radiative cooling rate; Fig. 7b) and/or in the static-stability ( $S$ ; Fig. 7a). Thus, in order to understand the reasons behind the decrease in  $D_r$  with  $N_a$  (for a given SST), in Fig. 9 we calculate the change in  $D_r$  with  $N_a$  for the different SSTs, assuming that either  $Q_r$  or  $S$  are held fixed at the value it attains at a reference  $N_a$  of  $200 \text{ cm}^{-3}$  for each SST. This calculation is similar to that presented in Fig. 4 of Bony et al. (2016), but for changes in  $N_a$  instead of changes in SST. Fig. 9 illustrates that the reduction of  $D_r$  with an increase in  $N_a$  can mostly be attributed to changes in  $S$ . This result is illustrated by the consistent reduction in  $D_r$  with  $N_a$  for all SSTs when only  $S$  (or the

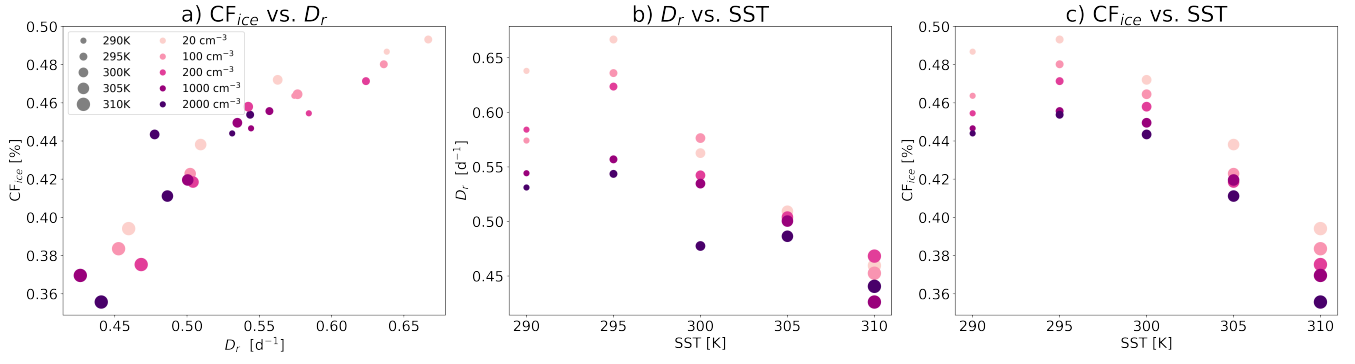


**Figure 8.** Changes in domain and time mean ice cloud fraction ( $CF_{ice}$ ) with  $D_r$  for the different simulations conducted under different  $N_a$  and SST (a), changes in  $D_r$  with SST (b), and changes in  $CF_{ice}$  with SST (c).

temperature –  $T$ ) is varied. However, when only  $Q_r$  is varied, the trend of  $D_r$  with  $N_a$  is not consistent across the different  
 270 SSTs, and for some of the SSTs, the trend is not monotonic.

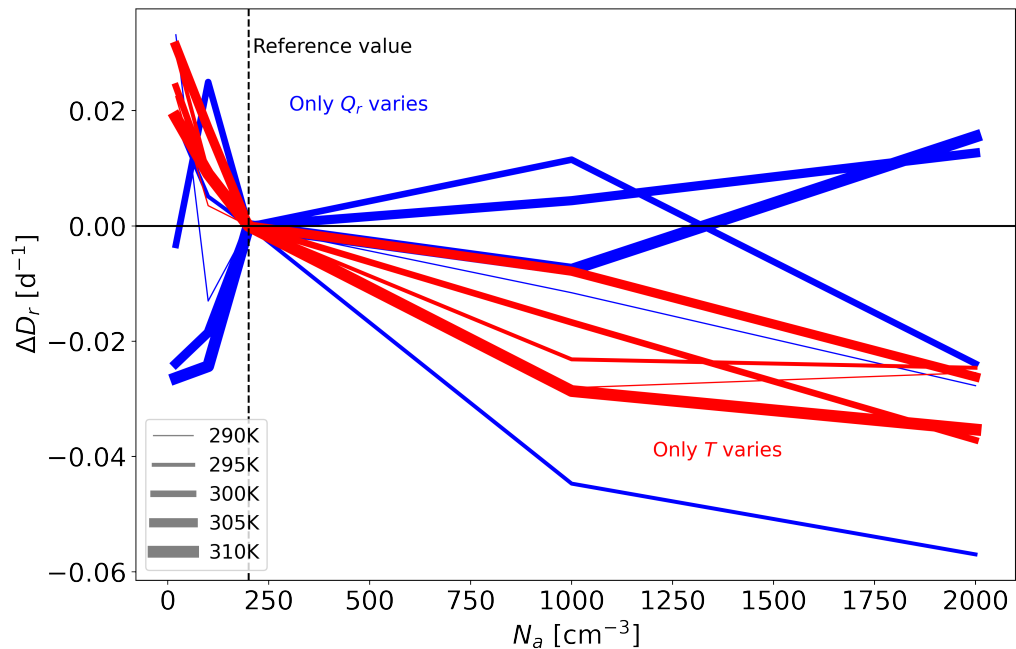


**Figure 9.** Relationship between the radiative-driven divergence ( $D_r$ ) and  $N_a$ , diagnosed by assuming that only either the temperature profile ( $T$  – red curves) or the clear-sky radiative cooling profile ( $Q_r$  – blue curves) vary with  $N_a$ . The reference for the  $T$  and  $Q_r$  are the simulations conducted under  $N_a = 200 \text{ cm}^{-3}$  (dashed vertical line) for each SST.

The domain and time mean temperature vertical profiles for the different simulations and their response to an increase in  $N_a$  is presented in Fig. 10. This figure illustrates that, for a given SST, an increase in  $N_a$  drives strong warming of the upper troposphere, and in some cases a weak cooling of the lower troposphere. This trend demonstrates an increase in  $S$  with  $N_a$ , which in turn explains the reduction in the anvil cloud fraction.

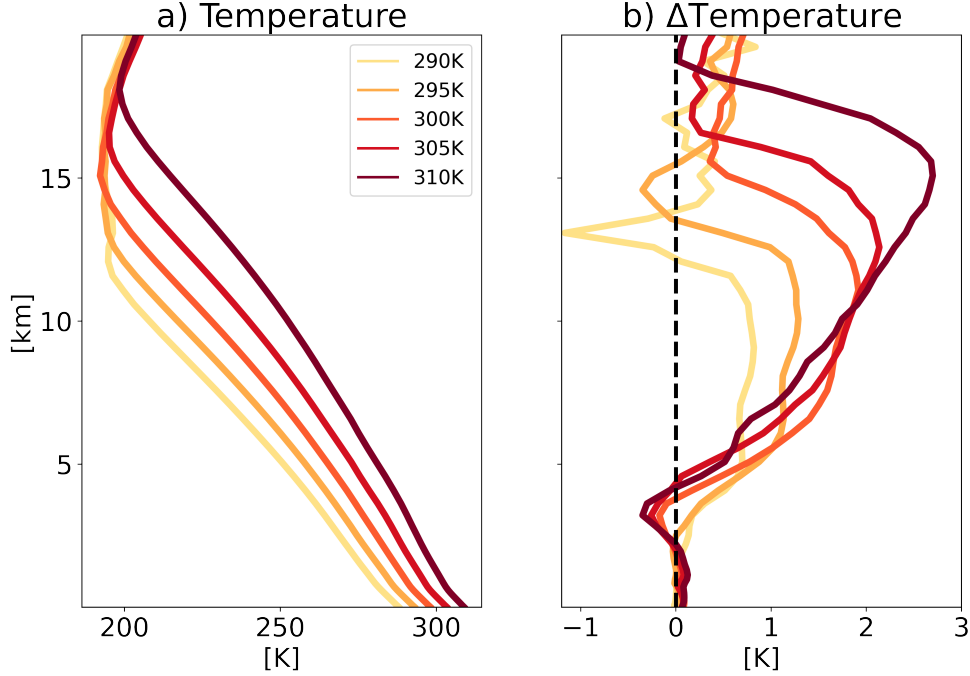


**Figure 10.** Domain and time mean vertical profiles of temperature of the cleanest runs ( $N_a = 20 \text{ cm}^{-3}$ ; **a**) and its response to increasing  $N_a$  to  $2000 \text{ cm}^{-3}$ , relative to the cleanest run of each SST (**b**). Here we only present the cleanest and the response of the most polluted runs for clarity. The full range of  $N_a$  is presented in Fig. S7, SI.

275 A remaining open question concerns the reasons behind the strong warming of the upper troposphere (or the increase in  $S$ ) with  $N_a$ . In the model, a central prognostic variable is the liquid/ice water static energy ( $h_L$ ). The  $h_L$  tendency equation contains 5 terms: advection (adv), radiation (rad), latent heating (includes latent heating from freezing), turbulence and large-scale tendency (Khairoutdinov and Randall, 2003). In an RCE configuration, by definition, the large-scale tendency is set to zero, thus having no effect here. In addition, in our simulations the turbulence term is negligible compared to the rest of  
 280 the terms. Hence, in Fig. 11 we present vertical profiles of the domain and time mean  $\frac{\partial h_L}{\partial t}$  due to latent heating, advection, and radiation of the different simulations. This figure illustrates that under equilibrium conditions, the latent heating acts to heat the upper troposphere, advection acts to cool it, although by a smaller magnitude, and radiation acts to weakly cool the entire troposphere almost uniformly. This trend is enhanced with an increase in  $N_a$  (Fig. 11d-f), suggesting that the increase

in temperature of the upper troposphere with  $N_a$  is mostly driven by a stronger latent heat release, which is consistent with the  
 285 higher production rates of graupel and snow with  $N_a$  (Figs. 3i and j). Graupel and snow, unlike small ice crystals, efficiently  
 sediment out of the cold portion of the cloud, thus leaving behind the heat they released in their formation, resulting in a net  
 warming effect. In addition, in higher altitudes, the air density drops. Thus, a given amount of latent heating will cause a larger  
 temperature change at higher altitudes than low altitudes (Gasparini et al., 2023). Therefore, higher production of graupel and  
 snow with  $N_a$  is identified as the main driver of the observed temperature increase in the upper troposphere.

### 290 3.4 Examining the surface precipitation response to aerosol perturbation using the atmospheric energy budget

Next, we examine the response of the surface precipitation to  $N_a$  under the different SSTs. Fig. 12a illustrates an increase in  
 surface precipitation (in energy units –  $L\Delta SP$ , where  $L$  is the latent heat of vaporization and  $SP$  is the surface precipitation)  
 with  $N_a$  across SSTs. In order to understand this increase, we use the atmospheric energy budget perspective (Muller and  
 O’Gorman, 2011; Dagan and Stier, 2020a; Williams et al., 2023) and decompose the changes in  $L\Delta SP$  to changes in LW  
 295 atmospheric radiative cooling ( $\Delta LWC$ , calculated as the TOA’s net LW radiation flux minus the surface’s net LW radiation  
 flux; Fig. 12b), changes in surface sensible heat flux ( $\Delta SHF$ ; Fig. 12c), and changes in atmospheric SW absorption ( $\Delta SWA$ ,  
 calculated as the TOA’s net SW radiation flux minus the surface’s net SW radiation flux; Fig. 12d), following the notations of  
 Williams et al. (2023):

$$L\Delta SP = \Delta LWC - \Delta SWA + \Delta SHF \quad (6)$$

We note that eq. 6 holds under equilibrium conditions, as simulated here (Muller and O’Gorman, 2011; Dagan and Stier,  
 300 2020a). Following the notations of eq. 6, Fig. 12a can be reconstructed by summing Fig. 12b-d. Hence, we note that the increase  
 in  $L\Delta SP$  could mostly be explained by enhanced  $\Delta LWC$  (Fig. 12b), while changes in  $\Delta SWA$  produce only a small positive  
 contribution, and changes in  $\Delta SHF$  present a small and non-consistent across SSTs contribution. The enhanced  $\Delta LWC$  with  
 $N_a$  is driven by clear-sky radiative cooling, which is in turn driven by the decreased  $CF_{ice}$  with  $N_a$  across SSTs, as illustrated  
 in Fig. 5a. The enhanced  $\Delta LWC$  is also consistent with the reduction in  $\Delta R^{LW}$  presented in Fig. 1b. These results suggest  
 305 that under equilibrium conditions, higher  $N_a$  concentrations drive higher LW cooling rates of the atmospheric column, which  
 supports the production of more precipitation.

## 4 Conclusions

Under anthropogenic-driven climate change, Earth’s energy budget is influenced by changes in the atmospheric composition,  
 including anthropogenic aerosols, which could affect the cloud radiative properties. In addition, changes in SST could drive  
 310 changes in the cloud radiative properties as well, which can in turn further change the SST. In this study, we investigate the  
 combined impact of SST and aerosol concentration ( $N_a$ ) on cloud properties in the framework of high-resolution radiative-  
 convective-equilibrium (RCE) simulations.

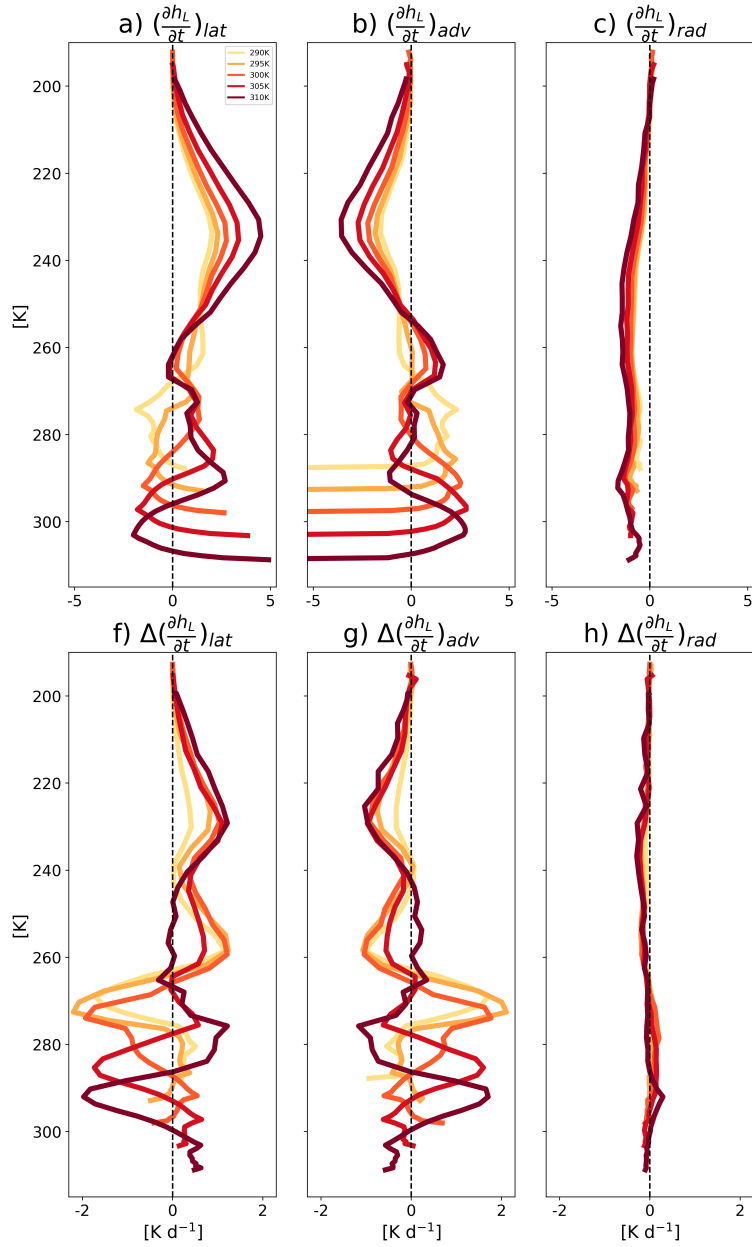


**Figure 11.** Vertical profiles of the domain and time mean tendency of the liquid/ice water static energy for the cleanest runs ( $N_a = 20 \text{ cm}^{-3}$ ) ( $h_L$ ) due to (a) latent heating, (b) advection, and radiation (c) in the different simulations conducted under different SST and  $N_a$ . Panels d – f present the response of these terms to increasing  $N_a$  to  $2000 \text{ cm}^{-3}$ , relative to the cleanest run for each SST. Here we only present the cleanest and the response of the most polluted runs for clarity. The full range of  $N_a$  is presented in Figs. S8 - S10, SI.

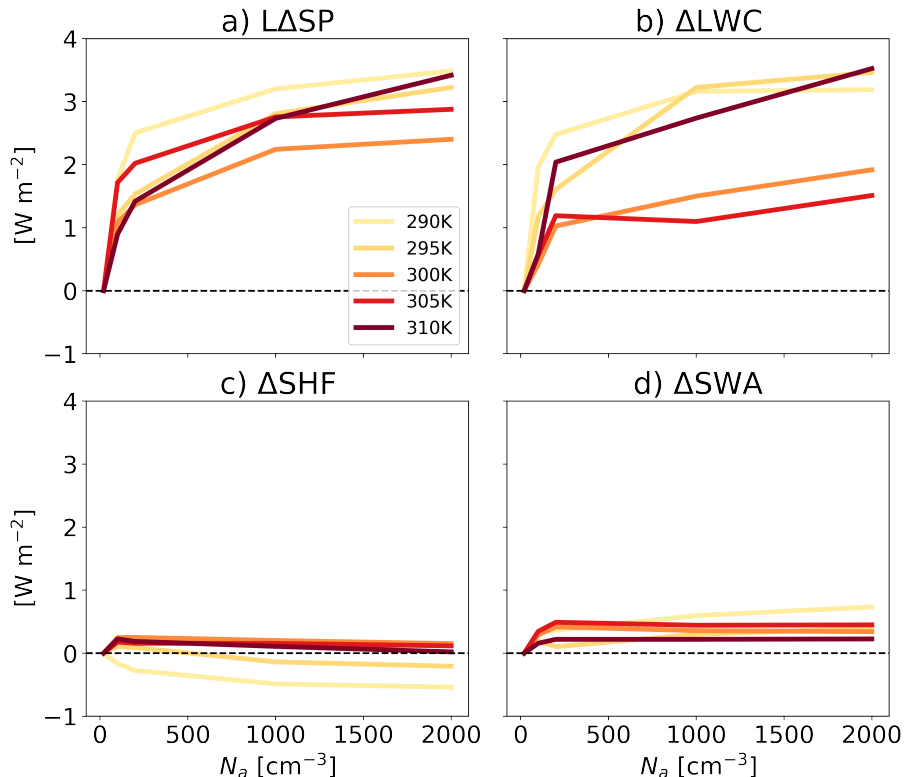


**Figure 12.** The response of domain and time mean surface precipitation ( $L\Delta SP$ ; **a**), longwave atmospheric radiative cooling ( $\Delta LWC$ ; **b**), surface sensible heat flux ( $\Delta SHF$ ; **c**) and atmospheric shortwave absorption ( $\Delta SWA$ ; **d**) to an increase in  $N_a$ , relative to the cleanest run for each SST ( $N_a = 20 \text{ cm}^{-3}$ ).

Using these idealized RCE simulations, we demonstrate that increasing  $N_a$ , which does not directly interact with radiation here, decreases top-of-atmosphere (TOA) energy gain across all SSTs, both in the longwave (LW) and shortwave (SW) parts of the spectrum, as a result of changes in the cloud radiative effect. We also show that this effect is stronger under lower SSTs, which is consistent with the stronger increase in liquid water path ( $\mathcal{L}$ ) with  $N_a$  under lower SSTs. The ice water path ( $\mathcal{I}$ ) and cloud fraction (CF) responses, on the other hand, are negative and consistent across SSTs.

To better understand these trends, we decompose the response of TOA energy gain ( $\Delta R$ ) to different cloud regimes (based on 2D histograms of  $\mathcal{L}$  and  $\mathcal{I}$ ) and to contributions from changes in the cloud opacity (the opacity term) and in cloud occurrence (the shift term) based on a linear decomposition. This decomposition illustrates that most of  $\Delta R$ 's negative trend and its SST-sensitivity is driven by the opacity term, which in turn is driven by the SW part of the spectrum. This trend can be explained by the Twomey effect, i.e. for a given  $\mathcal{L}$  and  $\mathcal{I}$  the clouds become more reflective with a rise in  $N_a$ . The Twomey effect is proportional to the baseline CF, thus becoming stronger under lower SST for which the baseline CF is higher. The shift term, on the other hand, illustrates a compensation between a positive response in the SW and a negative response in the LW, thus

325 producing a small net effect. Furthermore, we decompose  $\Delta R$  and its components per cloud regime, which illustrates that ice and shallow clouds are the main drivers behind the opacity and shift terms trends. Lastly, this cloud regime decomposition illustrates that, together with the general reduction in CF and specifically in ice cloud fraction ( $CF_{ice}$ ), an increase in  $N_a$  leads to the thinning of the ice clouds.

As has been previously reported (Bony et al., 2016), we observe a strong correlation between  $CF_{ice}$  and the maximum  
330 radiative-driven mass divergence at the upper troposphere ( $D_r$ ). We demonstrate that  $D_r$  generally decreases with  $N_a$  for a given SST, consistent with the reduction in  $CF_{ice}$  and the shift of the anvil clouds toward thinner clouds (Fig. 4). The reduction in  $D_r$  with an increase in  $N_a$  is shown here to be driven by an increase in static-stability at the upper troposphere under more polluted conditions (Fig. 9). The decrease in anvil cloud fraction with  $N_a$  across SSTs also leads to a decline in  $\mathcal{I}$ , causing an increase in the outgoing LW radiation, i.e., decreasing  $\Delta R^{LW}$ . This reduction in  $\Delta R^{LW}$  at the TOA directly increases LW  
335 cooling of the atmospheric column ( $\Delta LWC$ ), which, in turn, is identified as the main driver of enhanced surface precipitation ( $L\Delta SP$ ). We note that an increased surface precipitation could mean that aerosols get rained out faster, thus moderating the aerosol concentration. In our simulations  $N_a$  is prescribed, thus this feedback is disabled. This feedback should be examined in future studies.

Lastly, we try to explain the observed relative warming of the upper troposphere with  $N_a$ , which is consistent with the rise  
340 in static-stability, by examining the tendency equation of liquid/ice water static energy ( $\frac{dh_L}{dt}$ ). We demonstrate that the increase in static-stability with  $N_a$  can be explained by an increase in the latent-heating of the upper troposphere. Warm rain inhibition with  $N_a$  leads to heightened production rates of graupel and snow, which efficiently sediment out from the colder region of the cloud. As they descend, they leave behind the latent heat released during their formation, resulting in an overall warming effect and an increased stability.

345 The results presented here are based on idealized RCE simulations in a small domain, which suppress convective self-aggregation and large-scale circulation. Hence, in future work we aim to examine our conclusion in a set of simulations conducted using a channel domain, which includes interactions with larger scales. Furthermore, the role of other modeling choices, such as horizontal and vertical resolution and the role of boundary conditions (Dagan et al., 2022) in our results should be examined in future work. In addition, in this work we excluded aerosol-radiation interactions, which could drastically alter  
350 TOA energy gain (Bellouin et al., 2020; Williams et al., 2023), and as such could be of interest. Finally, our work is based on single-model simulations. An RCEMIP stage focusing on aerosol effect on clouds and RCE climate is currently being conducted. This set of multi-model simulations under harmonized setup will allow us to confront our conclusions with a large variety of models and microphysical schemes.

This work suggests that under equilibrium conditions, the magnitude of the effective radiative forcing by aerosol-cloud  
355 interactions decreases (becomes less negative) with an increase in SST. These results predict that under the ongoing global warming trend, the ability of aerosol-cloud-interactions to counteract some of the positive radiative forcing by greenhouse gasses will become smaller with time. In addition, it suggests that studying the sensitivity of clouds to aerosol and SST should be conducted concomitantly as mutual effects are expected.

*Code and data availability.* SAM is publicly available at: <http://rossby.msrc.sunysb.edu/marat/SAM.html> The data presented in this study  
360 is publicly available at: <https://doi.org/10.5281/zenodo.8338310>

*Author contributions.* SL carried out the simulations and analyses presented. GD assisted with the simulations. SL and GD designed and interpreted the analyses. SL prepared the manuscript with contributions from GD.

*Competing interests.* At least one of the (co-)authors is a member of the editorial board of Atmospheric Chemistry and Physics.

*Acknowledgements.* This research was supported by the Israel Science Foundation (grant number: 1419/21).



## 365 **References**

- Albrecht, B. A.: Aerosols, cloud microphysics, and fractional cloudiness, *Science*, 245, 1227–1230, 1989.
- Altaratz, O., Koren, I., Remer, L., and Hirsch, E.: Cloud invigoration by aerosols—Coupling between microphysics and dynamics, *Atmospheric Research*, 140, 38–60, 2014.
- Bellouin, N., Quaas, J., Gryspeerdt, E., Kinne, S., Stier, P., Watson-Parris, D., Boucher, O., Carslaw, K. S., Christensen, M., Daniau, A.-L.,  
370 et al.: Bounding global aerosol radiative forcing of climate change, *Reviews of Geophysics*, 58, e2019RG000 660, 2020.
- Beydoun, H. and Hoose, C.: Aerosol-Cloud-Precipitation Interactions in the Context of Convective Self-Aggregation, *Journal of Advances in Modeling Earth Systems*, 11, 1066–1087, <https://doi.org/https://doi.org/10.1029/2018MS001523>, 2019.
- Beydoun, H., Caldwell, P. M., Hannah, W. M., and Donahue, A. S.: Dissecting anvil cloud response to sea surface warming, *Geophysical Research Letters*, 48, e2021GL094 049, 2021.
- 375 Bony, S, D. J.-L. L. T. H. M. J.-J. S. C.: On dynamic and thermodynamic components of cloud changes, *Climate Dynamics*, <https://doi.org/10.1007/s00382-003-0369-6>, 2004.
- Bony, S., Stevens, B., Coppin, D., Becker, T., Reed, K. A., Voigt, A., and Medeiros, B.: Thermodynamic control of anvil cloud amount, *Proceedings of the National Academy of Sciences*, 113, 8927–8932, 2016.
- Carrió, G., , and Cotton, W.: Urban growth and aerosol effects on convection over Houston. Part II: Dependence of aerosol effects on  
380 instability, *Atmospheric research*, 102, 167–174, 2011.
- Ceppi, P., Brient, F., Zelinka, M. D., and Hartmann, D. L.: Cloud feedback mechanisms and their representation in global climate models, *Wiley Interdisciplinary Reviews: Climate Change*, 8, e465, 2017.
- Chen, Q., Koren, I., Altaratz, O., Heiblum, R. H., Dagan, G., and Pinto, L.: How do changes in warm-phase microphysics affect deep convective clouds?, *Atmospheric Chemistry and Physics*, 17, 9585–9598, 2017.
- 385 Choudhury, G. and Tesche, M.: A first global height-resolved cloud condensation nuclei data set derived from spaceborne lidar measurements, *Earth System Science Data*, 15, 3747–3760, <https://doi.org/10.5194/essd-15-3747-2023>, 2023.
- Christensen, M. W., Chen, Y.-C., and Stephens, G. L.: Aerosol indirect effect dictated by liquid clouds, *Journal of Geophysical Research: Atmospheres*, 121, 14–636, 2016.
- Christensen, M. W., Gettelman, A., Cermak, J., Dagan, G., Diamond, M., Douglas, A., Feingold, G., Glassmeier, F., Goren, T., Grosvenor,  
390 D. P., et al.: Opportunistic experiments to constrain aerosol effective radiative forcing, *Atmospheric chemistry and physics*, 22, 641–674, 2022.
- Collins, W. D., Rasch, P. J., Boville, B. A., Hack, J. J., McCaa, J. R., Williamson, D. L., Briegleb, B. P., Bitz, C. M., Lin, S.-J., and Zhang, M.: The formulation and atmospheric simulation of the Community Atmosphere Model version 3 (CAM3), *Journal of Climate*, 19, 2144–2161, 2006.
- 395 Dagan, G.: Equilibrium climate sensitivity increases with aerosol concentration due to changes in precipitation efficiency, *Atmospheric Chemistry and Physics*, 22, 15 767–15 775, 2022.
- Dagan, G. and Stier, P.: Constraint on precipitation response to climate change by combination of atmospheric energy and water budgets, *npj Climate and Atmospheric Science*, 3, 1–5, 2020a.
- Dagan, G. and Stier, P.: Ensemble daily simulations for elucidating cloud–aerosol interactions under a large spread of realistic environmental  
400 conditions, *Atmospheric Chemistry and Physics*, 20, 6291–6303, 2020b.

- Dagan, G., Koren, I., and Altaratz, O.: Aerosol effects on the timing of warm rain processes, *Geophysical Research Letters*, 42, 4590–4598, 2015.
- Dagan, G., Koren, I., Altaratz, O., and Heiblum, R. H.: Time-dependent, non-monotonic response of warm convective cloud fields to changes in aerosol loading, *Atmospheric Chemistry and Physics*, 17, 7435–7444, 2017.
- 405 Dagan, G., Koren, I., and Altaratz, O.: Quantifying the effect of aerosol on vertical velocity and effective terminal velocity in warm convective clouds, *Atmospheric Chemistry and Physics*, 18, 6761–6769, 2018.
- Dagan, G., Stier, P., Christensen, M., Cioni, G., Klocke, D., and Seifert, A.: Atmospheric energy budget response to idealized aerosol perturbation in tropical cloud systems, *Atmospheric Chemistry and Physics*, 20, 4523–4544, 2020.
- Dagan, G., Stier, P., Spill, G., Herbert, R., Heikenfeld, M., van den Heever, S. C., and Marinescu, P. J.: Boundary conditions representation  
410 can determine simulated aerosol effects on convective cloud fields, *Communications Earth & Environment*, 3, 71, 2022.
- Fan, J., Comstock, J. M., and Ovchinnikov, M.: The cloud condensation nuclei and ice nuclei effects on tropical anvil characteristics and water vapor of the tropical tropopause layer, *Environmental Research Letters*, 5, 044 005, 2010.
- Fan, J., Leung, L. R., Rosenfeld, D., Chen, Q., Li, Z., Zhang, J., and Yan, H.: Microphysical effects determine macrophysical response for aerosol impacts on deep convective clouds, *Proceedings of the National Academy of Sciences*, 110, E4581–E4590, 2013.
- 415 Freud, E. and Rosenfeld, D.: Linear relation between convective cloud drop number concentration and depth for rain initiation, *Journal of Geophysical Research: Atmospheres*, 117, 2012.
- Gasparini, B., Sokol, A. B., Wall, C. J., Hartmann, D. L., and Blossey, P. N.: Diurnal Differences in Tropical Maritime Anvil Cloud Evolution, *Journal of Climate*, 35, 1655 – 1677, <https://doi.org/10.1175/JCLI-D-21-0211.1>, 2022.
- Gasparini, B., Voigt, A., and et al., G. M.: Basic physics predicts stronger high cloud radiative heating with warming,  
420 <https://doi.org/https://doi.org/10.21203/rs.3.rs-2772229/v1>, 2023.
- Gottelman, A. and Sherwood, S. C.: Processes responsible for cloud feedback, *Current climate change reports*, 2, 179–189, 2016.
- Grabowski, W. W. and Morrison, H.: Untangling microphysical impacts on deep convection applying a novel modeling methodology. Part II: Double-moment microphysics, *Journal of the Atmospheric Sciences*, 73, 3749–3770, 2016.
- Gryspeerd, E. and Stier, P.: Regime-based analysis of aerosol–cloud interactions, *Geophysical research letters*, 39, 2012.
- 425 Harrop, B. E. and Hartmann, D. L.: Testing the Role of Radiation in Determining Tropical Cloud-Top Temperature, *Journal of Climate*, 25, 5731 – 5747, <https://doi.org/https://doi.org/10.1175/JCLI-D-11-00445.1>, 2012.
- Hartmann, D. L. and Berry, S. E.: The balanced radiative effect of tropical anvil clouds, *Journal of Geophysical Research: Atmospheres*, 122, 5003–5020, 2017.
- Hartmann, D. L. and Larson, K.: An important constraint on tropical cloud-climate feedback, *Geophysical research letters*, 29, 12–1, 2002.
- 430 Heikenfeld, M., White, B., Labbouz, L., and Stier, P.: Aerosol effects on deep convection: the propagation of aerosol perturbations through convective cloud microphysics, *Atmospheric Chemistry and Physics*, 19, 2601–2627, 2019.
- Igel, A. L. and van den Heever, S. C.: Invigoration or Enervation of Convective Clouds by Aerosols?, *Geophysical Research Letters*, 48, e2021GL093 804, 2021.
- Khairoutdinov, M. F. and Randall, D. A.: Cloud resolving modeling of the ARM summer 1997 IOP: Model formulation, results, uncertainties,  
435 and sensitivities, *Journal of the Atmospheric Sciences*, 60, 607–625, 2003.
- Koren, I., Kaufman, Y. J., Rosenfeld, D., Remer, L. A., and Rudich, Y.: Aerosol invigoration and restructuring of Atlantic convective clouds, *Geophysical Research Letters*, 32, 2005.
- Koren, I., Dagan, G., and Altaratz, O.: From aerosol-limited to invigoration of warm convective clouds, *science*, 344, 1143–1146, 2014.

- Koren, I., Altaratz, O., and Dagan, G.: Aerosol effect on the mobility of cloud droplets, *Environmental Research Letters*, 10, 104011, 2015.
- 440 Li, R., Storelvmo, T., Fedorov, A. V., and Choi, Y.-S.: A positive IRIS feedback: Insights from climate simulations with temperature-sensitive cloud–rain conversion, *Journal of climate*, 32, 5305–5324, 2019.
- Lindzen, R. S., Chou, M.-D., and Hou, A. Y.: Does the earth have an adaptive infrared iris?, *Bulletin of the American Meteorological Society*, 82, 417–432, 2001.
- Lutsko, N. J. and Cronin, T. W.: Increase in precipitation efficiency with surface warming in radiative-convective equilibrium, *Journal of*  
445 *Advances in Modeling Earth Systems*, 10, 2992–3010, 2018.
- Mauritsen, T. and Stevens, B.: Missing iris effect as a possible cause of muted hydrological change and high climate sensitivity in models, *Nature Geoscience*, 8, 346–351, 2015.
- Morrison, H., Curry, J., and Khvorostyanov, V.: A new double-moment microphysics parameterization for application in cloud and climate models. Part I: Description, *Journal of the atmospheric sciences*, 62, 1665–1677, 2005.
- 450 Muller, C. J. and Held, I. M.: Detailed investigation of the self-aggregation of convection in cloud-resolving simulations, *Journal of the Atmospheric Sciences*, 69, 2551–2565, 2012.
- Muller, C. J. and O’Gorman, P.: An energetic perspective on the regional response of precipitation to climate change, *Nature Climate Change*, 1, 266–271, 2011.
- Nesbitt, S. W. and Zipser, E. J.: The Diurnal Cycle of Rainfall and Convective Intensity according to Three Years of TRMM Measurements,  
455 *Journal of Climate*, 16, 1456 – 1475, [https://doi.org/10.1175/1520-0442\(2003\)016<1456:TDCORA>2.0.CO;2](https://doi.org/10.1175/1520-0442(2003)016<1456:TDCORA>2.0.CO;2), 2003.
- Nuijens, L. and Siebesma, A. P.: Boundary layer clouds and convection over subtropical oceans in our current and in a warmer climate, *Current Climate Change Reports*, 5, 80–94, 2019.
- Rasmussen, R. M., Geresdi, I., Thompson, G., Manning, K., and Karplus, E.: Freezing Drizzle Formation in Stably Stratified Layer Clouds: The Role of Radiative Cooling of Cloud Droplets, Cloud Condensation Nuclei, and Ice Initiation, *Journal of the Atmospheric Sciences*,  
460 59, 837 – 860, [https://doi.org/https://doi.org/10.1175/1520-0469\(2002\)059<0837:FDFISS>2.0.CO;2](https://doi.org/https://doi.org/10.1175/1520-0469(2002)059<0837:FDFISS>2.0.CO;2), 2002.
- Romps, D. M., Latimer, K., Zhu, Q., Jurkat-Witschas, T., Mahnke, C., Prabhakaran, T., Weigel, R., and Wendisch, M.: Air pollution unable to intensify storms via warm-phase invigoration, *Geophysical Research Letters*, p. e2022GL100409, 2023.
- Rosenfeld, D.: Suppression of rain and snow by urban and industrial air pollution, *science*, 287, 1793–1796, 2000.
- Rosenfeld, D., Lohmann, U., Raga, G. B., O’Dowd, C. D., Kulmala, M., Fuzzi, S., Reissell, A., and Andreae, M. O.: Flood or drought: how  
465 do aerosols affect precipitation?, *science*, 321, 1309–1313, 2008.
- Saint-Lu, M., Bony, S., and Dufresne, J.-L.: Observational evidence for a stability iris effect in the tropics, *Geophysical Research Letters*, 47, e2020GL089059, 2020.
- Seeley, J. T., Jeevanjee, N., Langhans, W., and Romps, D. M.: Formation of tropical anvil clouds by slow evaporation, *Geophysical Research Letters*, 46, 492–501, 2019.
- 470 Seidel, S. D. and Yang, D.: Temperatures of Anvil Clouds and Radiative Tropopause in a Wide Array of Cloud-Resolving Simulations, *Journal of Climate*, 35, 8065 – 8078, <https://doi.org/https://doi.org/10.1175/JCLI-D-21-0962.1>, 2022.
- Seifert, A. and Beheng, K.: A two-moment cloud microphysics parameterization for mixed-phase clouds. Part 2: Maritime vs. continental deep convective storms, *Meteorology and Atmospheric Physics*, 92, 67–82, 2006.
- Seinfeld, J. H., Bretherton, C., Carslaw, K. S., Coe, H., DeMott, P. J., Dunlea, E. J., Feingold, G., Ghan, S., Guenther, A. B., Kahn, R., et al.:  
475 Improving our fundamental understanding of the role of aerosol- cloud interactions in the climate system, *Proceedings of the National Academy of Sciences*, 113, 5781–5790, 2016.

- Sokol, Adam B., W. C. J. H. D. L.: Anvil cloud thinning implies greater climate sensitivity, [https://atmos.uw.edu/~abs66/docs/Sokol\\_et\\_al\\_2024\\_preprint.pdf](https://atmos.uw.edu/~abs66/docs/Sokol_et_al_2024_preprint.pdf), 2024.
- 480 Squires, P.: The microstructure and colloidal stability of warm clouds: Part I—The relation between structure and stability, *Tellus*, 10, 256–261, 1958.
- Squires, P. and Twomey, S.: The relation between cloud droplet spectra and the spectrum of cloud nuclei, *Geophysical Monograph Series*, 5, 211–219, 1960.
- Stevens, B. and Feingold, G.: Untangling aerosol effects on clouds and precipitation in a buffered system, *Nature*, 461, 607–613, 2009.
- Storer, R. L. and van den Heever, S. C.: Microphysical Processes Evident in Aerosol Forcing of Tropical Deep Convective Clouds, *Journal of the Atmospheric Sciences*, 70, 430 – 446, <https://doi.org/https://doi.org/10.1175/JAS-D-12-076.1>, 2013.
- 485 Twomey, S.: The nuclei of natural cloud formation part II: The supersaturation in natural clouds and the variation of cloud droplet concentration, *Geofisica pura e applicata*, 43, 243–249, 1959.
- Twomey, S.: Pollution and the planetary albedo, *Atmospheric Environment (1967)*, 8, 1251–1256, 1974.
- Twomey, S.: The influence of pollution on the shortwave albedo of clouds, *Journal of the atmospheric sciences*, 34, 1149–1152, 1977.
- 490 van den Heever, S. C., Stephens, G. L., and Wood, N. B.: Aerosol Indirect Effects on Tropical Convection Characteristics under Conditions of Radiative–Convective Equilibrium, *Journal of the Atmospheric Sciences*, 68, 699 – 718, <https://doi.org/https://doi.org/10.1175/2010JAS3603.1>, 2011.
- Varble, A.: Erroneous attribution of deep convective invigoration to aerosol concentration, *Journal of the Atmospheric Sciences*, 75, 1351–1368, 2018.
- 495 Williams, A. I., Watson-Parris, D., Stier, P., and Dagan, G.: Dependence of fast changes in global and local precipitation on the geographical location of aerosol absorption, *Authorea Preprints*, 2023.
- Williams, E., Rosenfeld, D., Madden, N., Gerlach, J., Gears, N., Atkinson, L., Dunnemann, N., Frostrom, G., Antonio, M., Biazon, B., et al.: Contrasting convective regimes over the Amazon: Implications for cloud electrification, *Journal of Geophysical Research: Atmospheres*, 107, LBA–50, 2002.
- 500 Williams, I. N. and Pierrehumbert, R. T.: Observational evidence against strongly stabilizing tropical cloud feedbacks, *Geophysical Research Letters*, 44, 1503–1510, 2017.
- Wing, A. A., Reed, K. A., Satoh, M., Stevens, B., Bony, S., and Ohno, T.: Radiative–convective equilibrium model intercomparison project, *Geoscientific Model Development*, 11, 793–813, 2018.
- Wing, A. A., Stauffer, C. L., Becker, T., Reed, K. A., Ahn, M.-S., Arnold, N. P., Bony, S., Branson, M., Bryan, G. H., Chaboureaud, J.-P., et al.: 505 Clouds and convective self-aggregation in a multimodel ensemble of radiative-convective equilibrium simulations, *Journal of advances in modeling earth systems*, 12, e2020MS002 138, 2020.
- Yuan, T., Remer, L. A., Pickering, K. E., and Yu, H.: Observational evidence of aerosol enhancement of lightning activity and convective invigoration, *Geophysical Research Letters*, 38, 2011.
- Zelinka, M. D. and Hartmann, D. L.: Why is longwave cloud feedback positive?, *Journal of Geophysical Research: Atmospheres*, 115, 2010.
- 510 Zelinka, M. D. and Hartmann, D. L.: The observed sensitivity of high clouds to mean surface temperature anomalies in the tropics, *Journal of Geophysical Research: Atmospheres*, 116, 2011.